ARTICLES
https://doi.org/10.1038/s41567-019-0583-8
nature physics

Probing dense baryon-rich matter with virtual photons

The HADES Collaboration*

About 10 μs after the Big Bang, the universe was filled—in addition to photons and leptons—with strong-interaction matter consisting of quarks and gluons, which transitioned to hadrons at temperatures close to $kT = 150$ MeV and densities several times higher than those found in nuclei. This quantum chromodynamics (QCD) matter can be created in the laboratory as a transient state by colliding heavy ions at relativistic energies. The different phases in which QCD matter may exist depend for example on temperature, pressure or baryochemical potential, and can be probed by studying the emission of electromagnetic radiation. Electron–positron pairs emerge from the decay of virtual photons, which immediately decouple from the strong interaction, and thus provide information about the properties of QCD matter at various stages. Here, we report the observation of virtual photon emission from baryon-rich QCD matter. The spectral distribution of the electron–positron pairs is nearly exponential, providing evidence for a source of temperature in excess of 70 MeV with constituents whose properties have been modified, thus reflecting peculiarities of strong-interaction QCD matter. Its bulk properties are similar to the dense matter formed in the final state of a neutron star merger, as apparent from recent multimessenger observation.

The motivation to study the properties of transient states of QCD matter under extreme conditions of temperature and density has many facets; for example, a plasma of quarks and gluons transitioned into nucleons and other hadronic bound states in the early universe. Similar states of matter, at lower temperatures, are believed still to exist in the interior of compact stellar objects, such as neutron stars. The formation of such cosmic matter in heavy-ion collisions provides access to studies of the microscopic structure of QCD matter at the femtoscale.

The different phases in which QCD matter may exist depend, as for any other known substance, on state variables such as temperature, pressure or chemical potentials. The phase diagram of QCD matter, indicating the conjectured phase boundaries in a graph correlating temperature (T) and baryochemical potential (μ_B), is shown in Fig. 1. The situation for symmetric matter ($\mu_B = 0$), where matter is balanced by antimatter, has recently been elaborated in ref. [1]. It is characterized by a crossover between ordinary hadronic matter and a new phase of strong-interaction matter—the quark–gluon plasma (QGP). By evaluating QCD it has been found that the crossover occurs around temperatures of about 155 MeV (refs. [2,3]), indicated in Fig. 1 by a yellow band. The crossover is quantified by the expectation value of a quantity called scalar antiquark–quark or chiral condensate ($\langle\bar{q}q\rangle$), the order parameter of dynamically broken chiral symmetry, as shown in the figure by blue curves (with labels). The behaviour of the chiral condensate at finite T and μ_B is of fundamental interest since it provides a description of chiral-symmetry restoration, a symmetry-conserving handedness in the strong interaction in the limit of massless quarks. The chiral symmetry is spontaneously broken in vacuum, and, as such, is responsible for the occurrence of nearly massless Goldstone bosons (the pions) and a large mass splitting of chiral-partner states in the light-hadron spectrum[4].

The conditions for chiral-symmetry restoration and deconfinement of hadrons into quarks and gluons in baryon-dominated matter (that is, $\mu_B > 0$) are not (yet) accessible by first-principle QCD calculations. It is currently believed that collisions of heavy ions at energies of a few gigaelectronvolts per nucleon do not produce matter under conditions that suffice to liberate the constituent quarks. Yet, a (partial) restoration of the chiral symmetry is predicted for baryon-rich matter already at moderate temperatures $kT \lesssim 100$ MeV, as the chiral condensate is substantially reduced in the fraction of volume occupied by baryons. Hence, a substantial modification of the masses and decay widths of hadronic states in such a medium is expected.

The experimental approach to explore the QCD phase diagram is to probe different regions with heavy-ion collisions by varying the collision energy and geometry. As an example, chemical freeze-out conditions ($T_{\mathrm{f.o.}}$, $\mu_{\mathrm{B\,f.o.}}$), extracted from a statistical model applied to the final hadron abundances, have been obtained from the Large Hadron Collider down to SIS18 energies (beam energy accessible by the 18 T m heavy-ion synchrotron at GSI, Darmstadt), as depicted in Fig. 1 (black symbols). They locate the position in the phase diagram that determines the hadronic composition of the matter observed in the detector. These points line up along a narrow band that spans the phase diagram and terminates at vanishing baryochemical potential at the limiting temperature characteristic of the crossover from hadrons to deconfined matter. However, many observational challenges remain, such as the search for the onset of the QGP at high μ_B, the location of the conjectured QCD critical point or the study of microscopic properties of matter.

Among all observables, photons and dileptons have the distinctive feature of being emitted throughout the evolution of the collision zone, thus probing the hot and dense phases in a way that no other known observable in heavy-ion collisions can. Dileptons emerge from the decay of photons, immediately decouple from the strong interaction and carry additional information that cannot be detected by hadrons. The temperatures obtained from the spectral distribution of virtual photons, indicated in Fig. 1 by red triangles, clearly demonstrate the penetrating nature of this radiation. Therefore, dileptons are ideal messengers of modifications of hadron properties, and even their 'melting' in the medium, and thus provide valuable information about QCD matter under extreme conditions.

*A full list of authors and affiliations appears in the online version of this paper.

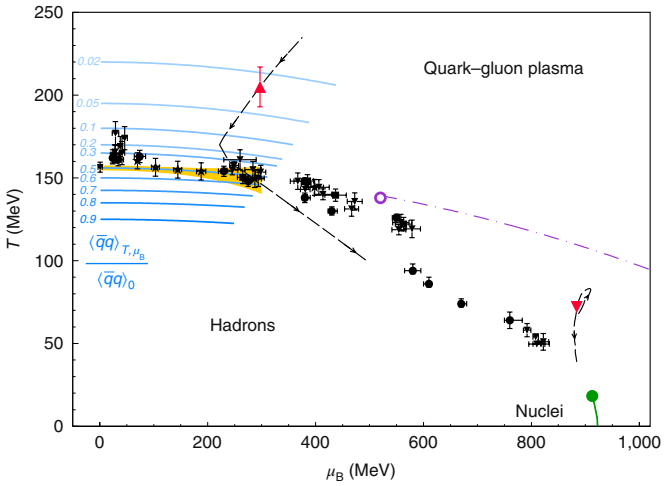

Fig. 1 | The conjectured QCD phase diagram of strong-interaction matter. The black symbols are the experimentally deduced chemical freeze-out points describing the final-state hadron abundances in a statistical hadronization model[1]. Stars, squares, circles and triangles depict results from the various implementations (related to canonical suppression of strangeness or the hadron spectrum). The horizontal and vertical bars are the s.d. due to experimental uncertainties. The expectation values of the chiral condensate relative to the vacuum as constrained by QCD (ref. [2]) are depicted as blue curves. The yellow band is the crossover region[3]. The dotted–dashed purple curve shows the conjectured first-order phase transition, which terminates in a second-order QCD critical point (open purple circle). The red upright triangle displays the temperature deduced from the dimuon invariant-mass spectrum measured by the NA60 Collaboration[14], while the red inverted triangle is the result of the HADES Collaboration, reported here. The two black dashed curves indicate the corresponding predicted evolution of the fireball parameters[43–45]. The solid green curve marks the first-order liquid–gas phase transition in nuclear matter, terminating in the critical end point (green circle)[46].

Here we report the first observation of dilepton emission from QCD matter at high net baryon density, which resembles in its properties the matter expected to be formed in binary neutron star mergers.

Thermal dilepton radiation

Dileptons (e^+e^-, or $\mu^+\mu^-$) emerge from the decay of virtual photons that directly couple to the electromagnetic current of hadrons. It has been argued that the spectral distribution of dileptons emitted during the early stage of a heavy-ion reaction at ultrarelativistic collision energies should reveal the thermal properties of the medium due to their production in frequent annihilations of quarks and antiquarks[5]. The eightfold differential emission rate of dileptons from a thermalized source (emissivity) per unit volume and time d^4x, and in a four-momentum interval d^4q, is related to the spectral function of the electromagnetic current in the medium $\Pi_{\mathrm{em}}(M, q; T, \mu_B)$:

$$\frac{\mathrm{d}N}{\mathrm{d}^4q\,\mathrm{d}^4x} = -\frac{\alpha^2}{\pi^3 M^2} f^{\mathrm{BE}}(q_0, T)\,\mathrm{Im}\,\Pi_{\mathrm{em}}(M, q; T, \mu_B) \qquad (1)$$

Here, $M \equiv M_{ee}$ is the invariant mass of the lepton pair with four-momentum $q = (q_0, \mathbf{q})$, $f^{\mathrm{BE}}(q_0, T)$ the Bose–Einstein distribution characterizing the thermalized medium and α the fine-structure constant. In this way, the spectral function encodes the microscopic properties of the medium at given T and μ_B. The dilepton yield observed in an experiment is then given by the spacetime integral over the full evolution of the radiating fireball. The strong temperature dependence of the emissivity, nevertheless, favours emission from the hot and dense stage of the collision.

The electromagnetic current is well known in vacuum. Its structure suggests a decomposition into a non-perturbative low-mass regime saturated by hadronic resonances, with the short-lived ρ meson playing the dominant role (in accordance with vector meson dominance[6]), and a high-mass regime, where perturbative (partonic) processes start to dominate. By selecting different regions in invariant mass the sensitivity of the experiment can be adjusted to the hadronic or partonic stage of the fireball evolution.

In the QGP the dilepton rate is chiefly determined by quark–antiquark annihilation[7]. If the emitting source has hadronic constituents, the dominant channel producing dileptons is the intermediate ρ meson[8,9]. Thus, the direct link between the spectral properties of the ρ meson and dilepton emission qualifies dilepton spectroscopy as ideal tool to probe the in-medium properties of hadrons. According to equation (1), modifications of the in-medium ρ spectral function should be imprinted in the spectral distribution of the dileptons at invariant masses around the vector meson's pole mass. It has been suggested in ref. [9] that the ρ mesons undergo a significant broadening in a hadronic medium, giving rise to abundant emission of dileptons at masses below the ρ pole mass[10]. This broadening is due to frequent interactions of the ρ meson with the surrounding hadrons in the medium—most importantly baryons.

The strong modification of the ρ might be a signal for the onset of chiral-symmetry restoration. The (partial) restoration of the dynamically broken chiral symmetry can be demonstrated by calculating the QCD partition function at high temperatures for a matter–antimatter-symmetric ($\mu_B = 0$) medium[11]. The restoration is accompanied by the melting of $\langle\bar{q}q\rangle$. This finding is consistent with the conclusion of the Weinberg sum rules, which state that the spectral properties of the vector meson ρ and its chiral partner, the axial-vector meson a_1, should become mass degenerate in the case of vanishing $\langle\bar{q}q\rangle$. Such a trend has been demonstrated in ref. [12] on the basis of QCD and Weinberg sum rules and is also supported by a calculation in the functional renormalization group framework[13]. In both cases, the degeneracy is realized through strong broadening of the chiral partners. As a fundamental property this degeneracy is expected to occur also in baryon-rich matter, which is not directly accessible by lattice QCD computations.

According to equation (1), if $\mathrm{Im}\,\Pi_{\mathrm{em}}/M^2$ is approximately constant, the dilepton emission rate is determined essentially by f^{BE} and is ideally suited to extract the temperature of the emitting medium (thermometer)[14,15]. Since the invariant mass is a Lorentz-invariant quantity, this observable is not affected by the rapid expansion of the fireball (the spectra of real photons are Doppler shifted). Due to the penetrating nature of dileptons, their yield in the low-mass region ($0.3 \leq M_{ee}$ (GeV c^{-2}) ≤ 0.7) depends on both the volume V and the lifetime τ of the fireball. The volume is also accessible through hadronic observables; dileptons are therefore sensitive in particular to the lifetime of the fireball (clock). This sensitivity has been demonstrated by model calculations[15–17]. The spectral distribution of the dileptons in the region around the low-mass vector mesons depends on the in-medium spectral function of the ρ and hence opens a window to the observation of chiral-symmetry restoration (spectrometer).

In the following we will show that the acceptance-corrected excess dilepton yield, obtained for the heavy collision system Au + Au at a centre-of-mass energy per colliding nucleon pair of $\sqrt{s_{\mathrm{NN}}} = 2.42$ GeV, is in accordance with emission from thermalized hadronic matter and with the assumption of a strong modification of hadronic states in a hot and dense medium.

Previous experiments

Significant excess radiation of dileptons in high-energy nuclear collisions, beyond contributions from final-state hadron decays, has

previously been observed in Super Proton Synchrotron/CERN (European Centre for Particle Physics)[18–20] and Relativistic Heavy-Ion Collider/Brookhaven National Laboratory[21–23] experiments. With the high-precision $\mu^+\mu^-$ data taken by the NA60 Collaboration in In+In collisions[20] it could be shown that thermal medium radiation, with invariant masses below 1 GeV c^{-2}, can be understood as radiation originating from strongly modified ρ-meson states formed and propagating in a hot hadronic environment. Such a strong modification had been conjectured before and explained as being due to the coupling of the ρ meson to baryons[9,24–26]. The good statistics of the NA60 data, even for invariant masses beyond the low-mass vector-meson pole region ($M_{ee}>1.2$ GeV c^{-2}), enabled us to extract an average source temperature of $kT=205\pm12$ MeV (ref. [14]), pointing to a mostly partonic medium as the source of this radiation (compare Fig. 1).

Low-mass dilepton emission at beam energies around 1 GeV per nucleon in elementary and in light heavy-ion collision systems has so far been studied by the DLS[27,28] and High Acceptance Dielectron Spectrometer (HADES)[29–33] experiments. The common striking feature observed at these energies is an enhanced yield of e^+e^- pairs above the contribution from η Dalitz decays and a strong isospin dependence in both η production and nucleon–nucleon (NN) bremsstrahlung[29,30]. Emission of e^+e^- from the internal charged pion exchange line—contributing only in $n+p$ collisions—has been proposed to be responsible for the isospin effect[29]. In the following, we will call these contributions 'conventional sources'. First indications for radiation beyond the conventional sources described above were found for the 48% most central Ar+KCl collisions with a mean number of participating nucleons $\langle A_{\mathrm{part}}\rangle=38.5$ (ref. [33]).

The HADES experiment

The experiment was performed with HADES at GSI using a beam of accelerated Au ions impinging on a stack of Au foils. A photograph and a cross-sectional view of the set-up are exhibited in Supplementary Figs. 1 and 2, respectively. A description of the relevant components (mini drift chamber, ring-imaging Cherenkov (RICH), time of flight and resistive plate chamber) can be found in Methods.

Using the measured momenta of electrons and positrons forming correlated e^+e^- pairs, various pair observables such as invariant mass, rapidity and transverse momentum were constructed and investigated. To obtain the signal-pair yield, the contribution of uncorrelated pairs was subtracted from the spectra of total pair yield. The signal spectrum was furthermore corrected for detector inefficiencies. Details of the analysis procedures are explained in Methods.

The resulting invariant-mass distribution of signal dielectrons, derived for the 40% most central Au+Au collisions, is shown in Fig. 2. The precision of the measurement is demonstrated by quoting the 1σ statistical uncertainty (s.d.) and our estimator for the systematic uncertainty (see Methods for details). The signal yield is normalized to the number of produced neutral pions to remove a trivial system-size dependence of the signal-pair yield. The pion multiplicities are found to scale linearly with $\langle A_{\mathrm{part}}\rangle$. For the centrality class presented here $\langle A_{\mathrm{part}}\rangle$ amounts to 173. At low invariant masses a contribution from three-body π^0 Dalitz decays is visible. Above $M_{ee}\simeq0.15$ GeV c^{-2}, the spectrum drops nearly exponentially over almost four orders of magnitude until it runs out of statistics around 1 GeV c^{-2}. Also shown are the expected yields attributed to mesons (π^0, η, ω, ρ^0, ϕ) decaying after they have decoupled from the fireball. Although dileptons radiated from this stage are not considered part of the thermal emission from the fireball, they still contribute to the total reconstructed signal-pair yield. Likewise, non-equilibrium contributions from baryonic sources (NN bremsstrahlung, Δ Dalitz decay), which contribute significantly at SIS18 energies[33], are also accounted for.

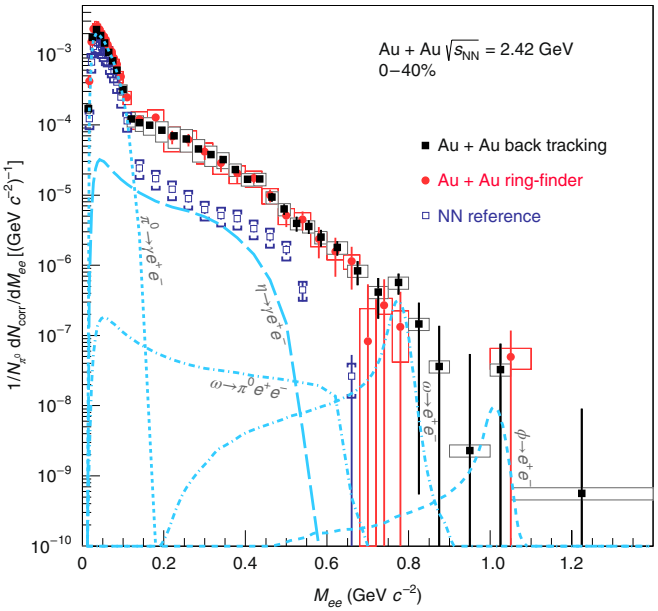

Fig. 2 | Reconstructed e^+e^- mass distribution from Au+Au collisions. Signal-pair invariant-mass distributions obtained from two different analysis strategies explained in the Methods: back tracking and ring-finder. The data are efficiency corrected and normalized to the number of neutral pions produced. Statistical (s.d.) and systematic uncertainties of the measurements are shown as vertical bars and boxes, respectively. The systematic uncertainties include uncertainties from subtraction of the CB, efficiency corrections, normalization to the number of π^0 and uncertainties of the cocktail components. Curves represent the π^0, η and ω Dalitz components, as well as ω and ϕ direct decays after decoupling from the fireball. Blue open squares show the NN reference spectrum. The sum of the two is the conventional sources contributing to the total signal yield.

This yield is approximated by the NN reference spectrum (open dark-blue squares) derived from measured $p+p$ and $n+p$ data[29] as

$$\frac{\mathrm{d}N^{\mathrm{NN}}_{\mathrm{ref}}}{\mathrm{d}M_{ee}}=\left(0.54\frac{\mathrm{d}N^{pp}}{\mathrm{d}M_{ee}}+0.46\frac{\mathrm{d}N^{np}}{\mathrm{d}M_{ee}}\right)\langle A_{\mathrm{part}}\rangle \qquad (2)$$

with prefactors reflecting the isospin composition of the Au+Au collision system. Note that the η contribution has already been removed from the NN reference, since this contribution is taken care of by the mesonic cocktail. While the Au+Au signal-pair yield and NN reference agree in the π^0 Dalitz region ($M_{ee}<0.15$ GeV c^{-2}) as expected, they differ strikingly for masses $M_{ee}>0.15$ GeV c^{-2}. In this region, the yield from Au+Au collisions exceeds the NN reference and mesonic cocktail substantially, clearly indicating the presence of excess radiation originating from the dense hadronic medium.

Excess radiation

To isolate this excess radiation we first subtract the contributions from conventional sources (compare equation (2) and Fig. 2). We further apply a mass-dependent acceptance correction factor in analogy to the efficiency correction explained in Methods. The resulting dilepton excess radiation is presented in Fig. 3. It exhibits a near-exponential fall-off. A fit of $\mathrm{d}N/\mathrm{d}M_{ee}\propto(M_{ee})^{3/2}\exp(-M_{ee}/T)$ (black-body spectral distribution) to the data gives a satisfactory overall description of the distribution and yields an inverse slope parameter of $kT=71.8\pm2.1$ MeV (reduced chi-square $\chi^2/\mathrm{ndf}=13.2/17$). This fit is justified because $\mathrm{Im}\,\Pi_{\mathrm{em}}/M^2$ is constant

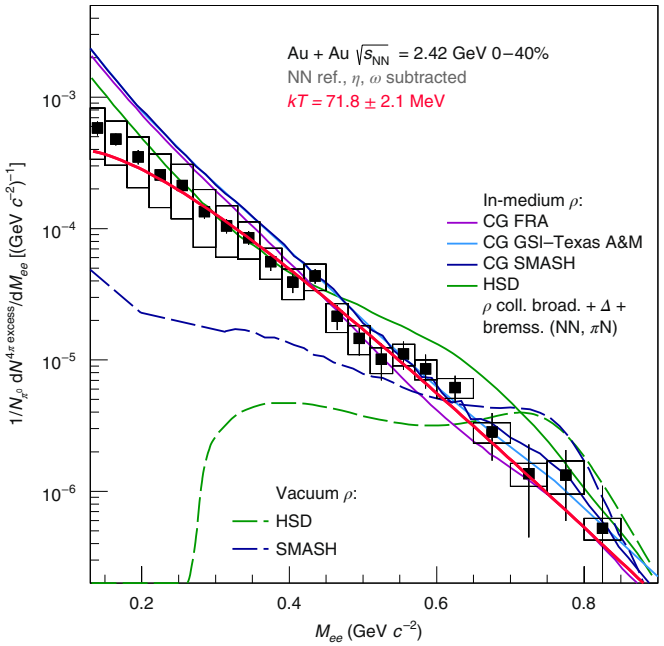

Fig. 3 | Acceptance-corrected dilepton excess yield. Black squares: excess yield extracted by subtracting η, ω contributions as well as the NN reference normalized to the number of neutral pions. Red curve: $dN/dM_{ee} \propto (M_{ee})^{3/2} \exp(-M_{ee}/T)$ fit. Dashed curves: ρ ('free' spectral function) contribution from HSD[34] and from SMASH[36] transport model calculations normalized to the respective number of neutral pions. The meaning of the errors is as in Fig. 2. Solid green curve: incoherent sum of $\Delta \rightarrow Ne^+e^-$, NN and πN bremsstrahlung and ρ (collisional broadening scenario) contributions from HSD (multiple Δ regenerations are assumed in the model). The dark-blue[36], blue[37] and pink[38] curves show the results of three versions of coarse-grained calculations using different concepts to obtain the local thermal parameters.

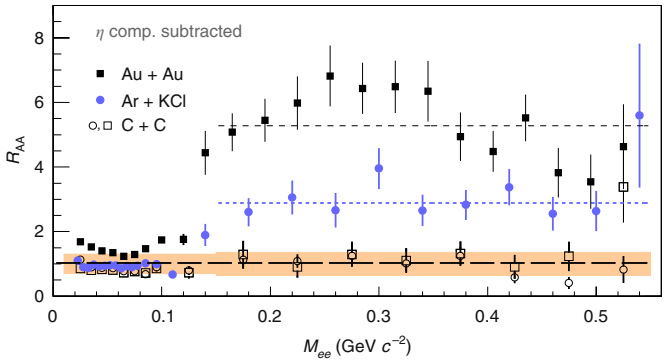

Fig. 4 | Systematics of the e^+e^- pair yield in A + A collisions attributed to excess radiation. The ratios (R_{AA}) depicted as symbols show the invariant-mass yield for various collision systems A + A (refs. [31,32]), per $\langle A_{part} \rangle$ of the respective heavy-ion centrality class, and normalized to the reference NN yield obtained from elementary NN collisions. Open black circles $R_{C+C\ 1A\ GeV}$, open black squares $R_{C+C\ 2A\ GeV}$, blue circles R_{Ar+KCl} and black squares R_{Au+Au}. Statistical (s.d.) uncertainties are shown as vertical bars. The yellow band corresponds to the systematic uncertainties (meaning as in Fig. 2). Horizontal lines mark the corresponding average excess factors (see ref. [33] for details).

in the range of fit ($0.2 \leq M_{ee}$ (GeV c^{-2}) ≤ 0.7) and the spectrum is thus dominated by f^{BE} (compare equation (1)).

The integrated excess yield in the window $0.3 \leq M_{ee}$ (GeV c^{-2}) ≤ 0.7 is found to be $N^{4\pi}_{excess} = (1.07 \pm 0.06^{stat} \pm 0.2^{syst}) \times 10^{-4}$. The excess surpasses the conventional sources by an average factor of 5.7 ± 0.3^{stat} and reaches a factor of about 12 if the 10% most central events are selected. This rise reflects the increasing number of ρ generations in the case of a larger fireball volume and clearly signals a qualitative change in the nature of radiating sources, immanent to heavier collision systems.

The dynamics of heavy-ion collisions at bombarding energies of a few gigaelectronvolts per nucleon have successfully been addressed by microscopic transport models[34–36]. However, for the description of dilepton emission, these calculations usually do not treat modifications of the ρ meson explicitly on the level of in-medium spectral functions. As can indeed be seen in Fig. 3, transport calculations assuming a free ρ spectral function (Hadron String Dynamics (HSD), SMASH)[34,36] feature a clear bump around $M_{ee} = 0.7$ GeV c^{-2}, which is obviously not observed in the experimental data. The agreement between transport model calculations and data can, however, be improved by assuming a strong collisional broadening of the ρ spectral function as demonstrated in the case of the HSD transport model. Furthermore, in HSD, most of the yield at the lower invariant masses is saturated by the contribution from an incoherent summation over Δ, NN and πN bremsstrahlung processes.

On the other hand, the excess radiation can be satisfactorily described by assuming thermal emission rates folded with a spacetime evolution of the fireball derived from the coarse-grained respective transport calculations (UrQMD, SMASH)[36–38] (compare Thermal dilepton radiation). The structureless excess yield indicates a strong medium modification of the ρ meson, probably induced by the high baryon density. This is a remarkable observation, as model calculations, based on the same in-medium spectral function, precisely reproduce the excess radiation measured at much higher collision energies. Despite earlier concerns[39] about the applicability of this approach at low beam energies, the calculations agree well with data in the region $M_{ee} > 0.3$ GeV c^{-2} although they systematically overshoot the measurement for small invariant masses, an observation that needs to be further investigated.

Further evidence for the existence of thermal radiation is obtained from studying the system-size dependence of the dilepton radiation. In Fig. 4 we present yields of signal pairs obtained in A + A collisions divided by the respective expectation from conventional sources for three different collision systems according to

$$R_{AA} = \frac{1}{\langle A^{AA}_{part} \rangle} \frac{dN^{AA}}{dM_{ee}} \left(\frac{dN^{NN}}{dM_{ee}} \right)^{-1} \quad (3)$$

The excess is observable for invariant masses beyond the π^0 Dalitz region. While for the C + C collisions the ratio is still consistent with unity within systematic uncertainties, the radiation is enhanced by an average factor of three in the case of Ar + KCl collisions. The strongest excess is observed for Au + Au collisions. A comparison of coarse-grained transport model calculations with data in the moderately heavy Ar + KCl collision system, $\langle A_{part} \rangle = 38.5$, also demonstrates the limitations of using vacuum properties for the hadrons: agreement with data is indeed achieved only with explicit in-medium spectral functions[36,38,40].

Our results demonstrate that, although at the beam energies considered here only about 10% of the charged particles in the final state are mesons (chiefly pions), we nevertheless observe a strong excess of dileptons. Its yield exceeds the one expected from known sources by factors and reveals a spectral distribution well described by assuming decays of in-medium ρ mesons. The data support the assumption of a strong broadening, which can be connected to partial restoration of the dynamically broken chiral symmetry.

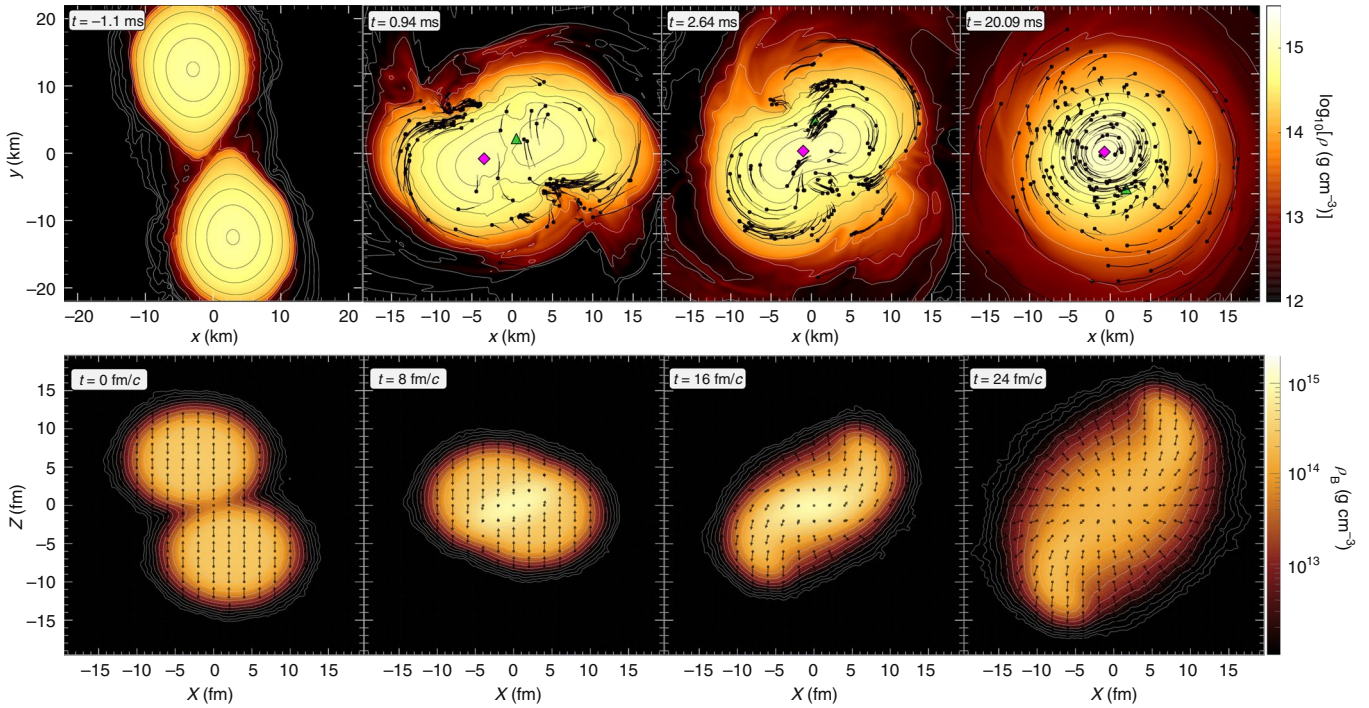

Fig. 5 | Simulations of nuclear matter in collisions yielding extreme conditions of density and temperature. Top row: simulation of a binary neutron star encounter of two neutron stars with equal masses of 1.35 $M_{\odot}$ finally merging into a single compact object[42] (size about 10 km in diameter, densities up to five times saturation density and temperatures reaching as high as 20 MeV). The matter is heated in the overlap zone and a superheated region surrounding the dense core is created about 20 ms after first contact, with densities about twice the saturation density and temperatures up to 75 MeV. The two neutron stars revolve (clockwise) around a common centre of mass. The green triangle marks the location where the maximum value of the temperature is reached, while the magenta diamond indicates that for density. Bottom row: time evolution of the energy density achieved in a non-central collision of two Au nuclei at an energy of 2.42 GeV per colliding nucleon pair. The *z* axis corresponds to the beam axis of the Au + Au collision. Densities reach up to three times the normal matter density and temperatures up to 80 MeV. The simulation is based on ref. [45]. Arrows depict local fluid flow velocities. While similar densities (see colour code bars) and temperatures are achieved, the displayed space and time scales are vastly different: kilometre for the neutron star merger simulation and femtometre in the case of the heavy-ion collision. Likewise, the collision events differ in duration by 20 orders of magnitude.

Prospects

The recently observed gravitational wave signals of a binary neutron star merger event opened a new era in multimessenger astronomy and possibly also a new avenue to connect stellar structures to the properties of the elementary building blocks of matter. Sophisticated model calculations show that postmerger neutron star configurations can develop a heated shell around the dense remnant core. In particular, they suggest that temperatures of 50–80 MeV and densities around twice the nuclear ground-state densities might be reached[41,42]. In Fig. 5 the panels show snapshots of the density evolution in the equatorial plane for characteristic stages of a binary neutron star merger (top row). They are conjoined with respective snapshots obtained from a simulation based on microscopic transport theory of the reaction investigated in this paper (bottom row). Recall that the average temperature of the radiating fireball formed in Au + Au collisions at $\sqrt{s_{\mathrm{NN}}} = 2.42$ GeV is found to be 71.8 ± 2.1 MeV. The transport models employed suggest that densities of up to three times the normal nuclear matter density are reached.

The space and time scales differ by typically 20 orders of magnitude, yet the matter properties in each system show striking similarities with respect to density and temperature. However, the equation of state of such forms of matter, which is of paramount importance for modelling merger/collision events, is not well constrained by theory. Among further quantities of high relevance are viscosities and conductivities, which are linked to real and virtual photon emissivities through a common theoretical basis. Therefore, the observation of thermal (virtual) photon emission from dense baryon matter in relativistic heavy-ion collisions serves as a benchmark for accessing other bulk properties.

To advance our understanding of the emissivity of strong-interaction matter under extreme conditions of temperature and density, it is important to extend such measurements to different collision energies. HADES will continue the investigations with substantially increased statistics, enabling access to the continuum radiation around $M_{ee} \geq 1$ GeV c^{-2} already at SIS energies. Experiments at the Relativistic Heavy-Ion Collider and the Large Hadron Collider with improved set-ups will scrutinize the conditions of matter at small baryon chemical potential. Future dilepton measurements at the Facility for Antiproton and Ion Research, Super Proton Synchrotron, Nuclotron-based Ion Collider Facility and Japan Proton Accelerator Research Complex Heavy Ion facilities will operate at interaction rates a factor of 100 higher than present facilities. They will enable multidifferential analyses with precision on the percentage level and thus help to improve our knowledge of chiral symmetry restoration in hot and dense matter and the QCD phase structure at high net baryon densities.

Online content

Any methods, additional references, Nature Research reporting summaries, source data, statements of code and data availability and associated accession codes are available at https://doi.org/10.1038/s41567-019-0583-8.

Received: 7 April 2018; Accepted: 5 June 2019;
Published online: 29 July 2019

References

1. Andronic, A., Braun-Munzinger, P., Redlich, K. & Stachel, J. Decoding the phase structure of QCD via particle production at high energy. *Nature* **561**, 321–330 (2018).
2. Borsanyi, S. et al. Is there still any T_c mystery in lattice QCD? Results with physical masses in the continuum limit III. *J. High Energy Phys.* **2010**, 73 (2010).
3. Bazavov, A. et al. Chiral crossover in QCD at zero and non-zero chemical potentials. *Phys. Lett. B* **795**, 15–21 (2019).
4. Roberts, C. D. Perspective on the origin of hadron masses. *Few Body Syst.* **58**, 5–17 (2017).
5. Shuryak, E. V. Quark-gluon plasma and hadronic production of leptons, photons and psions. *Phys. Lett. B* **78**, 150–153 (1978).
6. Kroll, N. M., Lee, T. D. & Zumino, B. Neutral vector mesons and the hadronic electromagnetic current. *Phys. Rev.* **157**, 1376–1399 (1967).
7. McLerran, L. D. & Toimela, T. Photon and dilepton emission from the quark–gluon plasma: some general considerations. *Phys. Rev. D* **31**, 545–602 (1985).
8. Gale, C. & Kapusta, J. I. Dilepton radiation from high temperature nuclear matter. *Phys. Rev. C* **35**, 2107–2116 (1987).
9. Rapp, R. & Wambach, J. Chiral symmetry restoration and dileptons in relativistic heavy ion collisions. *Adv. Nucl. Phys.* **25**, 1 (2000).
10. Pisarski, R. D. Phenomenology of the chiral phase transition. *Phys. Lett. B* **110**, 155–158 (1982).
11. Ding, H. T., Kaczmarek, O. & Meyer, F. Thermal dilepton rates and electrical conductivity of the QGP from the lattice. *Phys. Rev. D* **94**, 034504 (2016).
12. Hohler, P. M. & Rapp, R. Is ρ-meson melting compatible with chiral restoration?. *Phys. Lett. B* **731**, 103–109 (2014).
13. Jung, C., Rennecke, F., Tripolt, R. A., von Smekal, L. & Wambach, J. In-medium spectral functions of vector- and axial-vector mesons from the functional renormalization group. *Phys. Rev. D* **95**, 036020 (2017).
14. Specht, H. J. Thermal dileptons from hot and dense strongly interacting matter. *AIP Conf. Proc.* **1322**, 1–10 (2010).
15. Rapp, R. & van Hees, H. Thermal dileptons as fireball thermometer and chronometer. *Phys. Lett. B* **753**, 586–590 (2016).
16. Heinz, U. W. & Lee, K. S. The rho peak in the dimuon spectrum as a clock for fireball lifetimes in relativistic nuclear collisions. *Phys. Lett. B* **259**, 162–168 (1991).
17. Barz, H. W., Friman, B. L., Knoll, J. & Schulz, H. Production of phi, rho and omega mesons in the hadronization of a quark–gluon plasma. *Phys. Lett. B* **254**, 315–319 (1991).
18. Adamova, D. et al. Enhanced production of low mass electron pairs in 40-AGeV Pb–Au collisions at the CERN SPS. *Phys. Rev. Lett.* **91**, 042301 (2003).
19. Agakishiev, G. et al. Low mass e^+e^- pair production in 158/A-GeV Pb–Au collisions at the CERN SPS, its dependence on multiplicity and transverse momentum. *Phys. Lett. B* **422**, 405–412 (1998).
20. Arnaldi, R. et al. First measurement of the rho spectral function in high-energy nuclear collisions. *Phys. Rev. Lett.* **96**, 162302 (2006).
21. Adare, A. et al. Dielectron production in Au+Au collisions at $\sqrt{SNN} = 200$ Gev. *Phys. Rev. C* **93**, 014904 (2016).
22. Adamczyk, L. et al. Measurements of dielectron production in Au+Au collisions at $\sqrt{SNN} = 200$ Gev from the STAR experiment. *Phys. Rev. C* **92**, 024912 (2015).
23. Adam, J. et al. Measurements of dielectron production in Au + Au collisions at $\sqrt{SNN} = 27, 39$, and 62.4 GeV from the STAR experiment. Preprint at https://arxiv.org/abs/1810.10159 (2018).
24. Herrmann, M., Friman, B. L. & Nörenberg, W. Properties of rho mesons in nuclear matter. *Nucl. Phys. A* **560**, 411–436 (1993).
25. Chanfray, G. & Schuck, P. The Rho meson in dense matter and its influence on dilepton production rates. *Nucl. Phys. A* **555**, 329–353 (1993).
26. Peters, W., Post, M., Lenske, H., Leupold, S. & Mosel, U. The spectral function of the rho meson in nuclear matter. *Nucl. Phys. A* **632**, 109–127 (1998).
27. Wilson, W. K. et al. Inclusive dielectron cross-sections in p + p and p + d interactions at beam energies from 1.04-GeV to 4.88-GeV. *Phys. Rev. C* **57**, 1865–1878 (1998).
28. Porter, R. J. et al. Dielectron cross-section measurements in nucleus-nucleus reactions at 1-A/GeV. *Phys. Rev. Lett.* **79**, 1229–1232 (1997).
29. Agakishiev, G. et al. Origin of the low-mass electron pair excess in light nucleus-nucleus collisions. *Phys. Lett. B* **690**, 118–122 (2010).
30. Adamczewski-Musch, J. et al. Analysis of the exclusive final state npe^+e^- in quasi-free np reaction. *Eur. Phys. J. A* **53**, 149–161 (2017).
31. Agakichiev, G. et al. Dielectron production in C-12 + C-12 collisions at 2-AGeV with HADES. *Phys. Rev. Lett.* **98**, 052302 (2007).
32. Agakishiev, G. et al. Study of dielectron production in C + C collisions at 1-A-GeV. *Phys. Lett. B* **663**, 43–48 (2008).
33. Agakishiev, G. et al. Dielectron production in Ar + KCl collisions at 1.76A GeV. *Phys. Rev. C* **84**, 014902 (2011).
34. Bratkovskaya, E. L. et al. System size and energy dependence of dilepton production in heavy-ion collisions at 1-2 GeV/nucleon energies. *Phys. Rev. C* **87**, 064907 (2013).
35. Weil, J., van Hees, H. & Mosel, U. Dilepton production in proton-induced reactions at SIS energies with the GiBUU transport model. *Eur. Phys. J. A* **48**, 111–126 (2012).
36. Staudenmaier, J., Weil, J., Steinberg, V., Endres, S. & Petersen, H. Dilepton production and resonance properties within a new hadronic transport approach in the context of the GSI-HADES experimental data. *Phys. Rev. C* **98**, 054908 (2018).
37. Galatyuk, T., Hohler, P. M., Rapp, R., Seck, F. & Stroth, J. Thermal dileptons from coarse-grained transport as fireball probes at SIS energies. *Eur. Phys. J. A* **52**, 131–139 (2016).
38. Endres, S., van Hees, H., Weil, J. & Bleicher, M. Dilepton production and reaction dynamics in heavy-ion collisions at SIS energies from coarse-grained transport simulations. *Phys. Rev. C* **92**, 014911 (2015).
39. Lang, A. et al. Local thermodynamic properties and equilibration in relativistic heavy ion collisions. *Phys. Lett. B* **245**, 147–152 (1990).
40. Seck, F., Galatyuk, T., Rapp, R. & Stroth, J. Thermal dileptons as QCD matter probes at SIS. *J. Phys. Conf. Ser.* **1024**, 012011 (2018).
41. Bauswein, A., Goriely, S. & Janka, H.-T. Systematics of dynamical mass ejection, nucleosynthesis, and radioactively powered electromagnetic signals from neutron-star mergers. *Astrophys. J.* **773**, 78 (2013).
42. Most, E. R. et al. Signatures of quark-hadron phase transitions in general-relativistic neutron-star mergers. *Phys. Rev. Lett.* **122**, 061101 (2019).
43. Rapp, R. Hadro chemistry and evolution of (anti-) baryon densities at RHIC. *Phys. Rev. C* **66**, 017901 (2002).
44. Guenther, J. N. et al. The QCD equation of state at finite density from analytical continuation. *Nucl. Phys. A* **967**, 720–723 (2017).
45. Bass, S. A. et al. Microscopic models for ultrarelativistic heavy ion collisions. *Prog. Part. Nucl. Phys.* **41**, 255–369 (1998).
46. Floerchinger, S. & Wetterich, C. Chemical freeze-out in heavy ion collisions at large baryon densities. *Nucl. Phys. A* **890-891**, 11–24 (2012).

Acknowledgements

The collaboration gratefully acknowledges the support by PTDC/FIS/113339/2009 LIP Coimbra (Portugal), 2013/10/M/ST2/00042, 2016/23/P/ST2/040 POLONEZ, 2017/25/N/ST2/00580, 2017/26/M/ST2/00600 SIP JUC Cracow, National Science Centre (Poland), VH-NG-823, DFG GRK 2128, DFG CRC-TR 211, ExtreMe Matter Institute EMMI at the GSI, BMBF:05P18RDFC1 TU Darmstadt (Germany), EU FP7:283286, BMBF:05P12CRGHE HZDR Dresden (Germany), HIC for FAIR (LOEWE), GSI F&E, EMMI, BMBF:05P15RFFCA Goethe-Universität, Frankfurt (Germany), DFG EClust 153, GSI F&E:TMLRG1316F, BMBF:05P15WOFCA, SFB 1258, DFG FAB898/2-2 TU München, Garching (Germany), BMBF:05P12RGGHM JLU Giessen, Giessen (Germany), INFN-LNS Catania, Catania (Italy), Russian Academic Excellence 02.a03.21.0005, Minobrnauka 3.3380.2017/4.6 NRNU MEPhI Moscow (Russia), UCY/3411-23100, University Cyprus (Cyprus), CNRS/IN2P3 IPN Orsay (France), AS CR M100481202, GACR 13-06759S, MSMT LM2015049, PO VVV CZ.02.1.01/0.0/0.0/16_013/0001677 and MSMT LTT17003 NPI CAS Rez (Czech Republic).

Author contributions

All authors have contributed equally to the publication, being variously involved in the design and the construction of the detectors, writing software, calibrating subsystems, operating the detectors and acquiring data, and finally analysing the processed data.

Competing interests

The authors declare no competing interests.

Additional information

Supplementary information is available for this paper at https://doi.org/10.1038/s41567-019-0583-8.

Reprints and permissions information is available at www.nature.com/reprints.

Correspondence and requests for materials should be addressed to J.S.

Publisher's note: Springer Nature remains neutral with regard to jurisdictional claims in published maps and institutional affiliations.

Methods

The HADES apparatus. As shown in Supplementary Figs. 1 and 2, the HADES detector[47] features a six-coil superconducting toroidal magnet providing very good acceptance for charged particles emitted from the collision zone mostly at polar angles between 18° and 85°. Each sector of the resulting hexagonal detector volume is equipped with four planes of mini drift chambers (MDC), two in front of and two behind the magnetic field region. The tracking section is followed by a time-of-flight (TOF) system, composed of plastic scintillator strips covering angles above 45° and a resistive plate chamber (RPC), followed by an electromagnetic preshower detector (Shower), covering the region below.

The field-free region surrounding the target holds a RICH detector designed to selectively detect electrons and positrons by their Cherenkov emission (yellow lines). Ultrathin and radiation-hard segmented diamond detectors are installed in the beamline upstream of the target to provide precise time-zero information and to synchronize the reaction trigger. The set-up is complemented with a large-area scintillator hodoscope, placed 7 m downstream, which is used to provide additional event characterization, such as the centrality and reaction plane of each registered collision.

Event selection. Au + Au collisions investigated in this analysis were recorded by requiring a trigger of at least 20 hits in the time-of-flight detector system. This condition selects the class of the 40% most central Au + Au collisions, corresponding to reaction impact parameters $b \leq 9.3$ fm. The centrality classes are extracted from a detailed comparison of the observed charged-particle multiplicity distribution in HADES with both a Glauber Monte Carlo model and microscopic transport model calculations of the collision system[48]. The event sample used in the dilepton analysis amounts in total to 2.6×10^9 Au + Au collisions. Electron and positron track candidates were searched for and isolated by first matching (in space and time) high-quality particle tracks reconstructed in the mini drift chamber planes with a corresponding unique hit in the time-of-flight detectors. Next, e^- and e^+ were identified by requiring a matching ring pattern in the hadron-blind RICH detector. Finally, all possible pair combinations were formed, opposite sign and like sign, and the corresponding lepton pair four-momenta were calculated.

Reconstruction of pure electron/positron samples. To further improve the purity of e^+ and e^- candidates, alternative approaches were adopted, each of them trading efficiency against purity in different ways. In the standard approach, a series of independent conditions on the correlation of the particle velocity and momentum, the magnitude of the Shower signal and a refined declination of the RICH ring was required, as described in refs. [33,47]. The second approach (ring-finder[49]) combined these observables and further parameters defining the ring quality into an input vector of an artificial neural network (implemented in the ROOT toolkit for multivariate data analysis[50]). Signal and background samples were defined either by selecting high-purity samples from data or entirely on the basis of full Monte Carlo simulations employing dedicated digitizers to model the true detector response. A third procedure also used a neural network but did not require an identified ring in the RICH detector. Rather, the region of interest on the RICH photodetector plane was searched for signatures of a ring (back tracking[51]). The intersection of the track with the mirror was determined and the location of the expected ring centre on the photodetector plane was then calculated making use of the optical properties of the RICH. The latter procedure has particular advantages in the case of touching or overlapping rings, typical for pairs with opening angles $\alpha_{ee} < 4°$. In the final step of data processing, all identified e^- and e^+ candidates of a given event were combined to 'neutral' (unlike-sign) pairs. Most of these pairs, however, represent random combinations (that is they do not stem from the same virtual photon) and form the combinatorial background (CB).

Extraction of the pair signal. The dilepton spectrum was finally extracted by subtracting from the differential unlike-sign pair yield (N^{+-}) the distribution of the CB. To estimate the CB we employed the same-event like-sign method as $N^{\mathrm{CB}} = 2\kappa\,(N^{++}N^{--})^{0.5}$, where the factor κ accounts for a charge asymmetry of the spectrometer acceptance and reconstruction. κ was computed with the help of the event-mixing method using the relation $\kappa = N^{+-}_{\mathrm{mix}} / \left(N^{++}_{\mathrm{mix}} N^{--}_{\mathrm{mix}}\right)^{0.5}$. The event-mixed distributions generated from data and Monte Carlo simulation coincide, which benchmarks the correctness of efficiency modelling in the HADES Monte Carlo simulation. For $M_{ee} > 0.3$ GeV c^{-2}, where the statistics of the like-sign same-event background is limited, the mixed-event unlike-sign yield, scaled to the integral of the like-sign yield, was used. For invariant masses below 0.3 GeV c^{-2}, the same-event method was taken to properly account for correlated background. The finally obtained invariant-mass distributions for all pairs (N^{+-}) and background pairs (CB) are shown in Supplementary Fig. 3 for the back tracking analysis procedure. The raw signal emerges after subtracting N^{CB} from N^{+-}. Also depicted is the signal-to-background ratio (S/B), which reaches a minimum of 10% around $M_{ee} \simeq 0.25$ GeV c^{-2}. The signal spectrum contains 190,000 and 20,000 e^+e^- in the mass region below and above 0.15 GeV c^{-2}, respectively.

Correction for detector inefficiency. The signal distribution was further corrected for inefficiencies due to the detector response and inactive regions within the acceptance of the spectrometer (coil region, fiducial areas). To do this, individually simulated e$^-$ and e$^+$ tracks were generated in the acceptance and embedded into real events on an event-by-event basis. They were then reconstructed using the full analysis and reconstruction chain. For each three-dimensional phase space bin $\mathrm{d}^3p_{\mathrm{lab}} \propto \mathrm{d}p\,\mathrm{d}\theta\,\mathrm{d}\phi$ the ratio of the number of reconstructed leptons over those accepted within the HADES geometry was derived (single-lepton efficiency matrix). The pair invariant-mass signal was then corrected on the basis of on the single-lepton efficiency $\varepsilon^{\pm}(p,\theta,\phi)$ by deriving a correction vector $N_i^{\mathrm{corr}}(M) = N_i(M)/\hat{\varepsilon}_i$ with

$$\hat{\varepsilon}_i = \hat{\varepsilon}(M_i) = \frac{\int_{M_i}^{M_i+\Delta_i} \sum_n \varepsilon_n^+ \varepsilon_n^- \delta(M - M_n)\,\mathrm{d}M}{\int_{M_i}^{M_i+\Delta_i} \sum_n \delta(M - M_n)\,\mathrm{d}M} \tag{4}$$

where the sum is running over several sets (n) of simulated e^+e^- using various cocktail generators realized in the Pluto simulation package[52], $\varepsilon_n^{\pm} = \varepsilon^{\pm}(p_n, \theta_n, \varphi_n)$, M_n is the invariant mass of the simulated pair, and M_i and $\Delta_i = M_{i+1} - M_i$ are the position and width of the ith mass bin, respectively. The used source cocktail contained π^0, η and ω Dalitz decays, as well as a thermal ρ contribution. The systematic uncertainty in the efficiency determination due to our particular choice of cocktail was evaluated by alternatively taking dileptons from the microscopic transport code HSD. Differences in pair efficiency were found to be below 7% and smooth as a function of invariant mass (see the discussion of systematic uncertainties below).

We further apply a mass-dependent acceptance correction factor in analogy to the efficiency correction discussed above, but this time relating simulated pairs in the acceptance to all simulated pairs.

Hadron decay cocktail. The different meson multiplicities were determined as follows: (1) for the π^0 the charged pion multiplicities were used, that is $N_{\pi^0} \equiv \frac{1}{2}(N_{\pi^-} + N_{\pi^+}) = 8.65 \pm 0.39^{\mathrm{syst}} \pm 0.35^{\mathrm{extrap}}$, (2) the η multiplicity was obtained by an analysis of the same data set using the photon conversion method as $N_\eta = 0.11 \pm 0.01^{\mathrm{syst}} \pm 0.03^{\mathrm{syst}} \pm 0.01^{\mathrm{extrap}}$ (this value is consistent with the interpolated two-arm photon spectrometer measurement[53]), (3) the ϕ multiplicity was reconstructed through the K^+K^- decay channel as $N_\phi = (9.9 \pm 2.4^{\mathrm{syst}} \pm 1.0^{\mathrm{syst}} \pm 0.5^{\mathrm{extrap}}) \times 10^{-5}$ (ref. [54]) and (4) the ω multiplicity $N_\omega = (9.9 \pm 3.5) \times 10^{-3}$ was determined by fitting the acceptance-corrected invariant mass spectrum itself in the region $M_{ee} = 0.4$–1 GeV c^{-2} with the sum of a Gaussian and an exponential.

Estimation of systematic uncertainties. Systematic uncertainties are shown as boxes and are generally larger than statistical ones. They are due to variations observed in various analysis steps[49,51], namely the following.

- Subtraction of the CB brings an uncertainty of $0.02B/S$. This is the largest contribution to the systematic uncertainty.
- Calculating the single-lepton efficiency by embedding simulated electrons and positrons either into UrQMD events or into real events. This contribution was estimated bin by bin in pair observables and is smaller than 2%.
- Using different models to calculate one-dimensional efficiency and acceptance corrections. This contribution is calculated bin by bin in pair observables and introduces 4% at maximum in the case of efficiency correction and 7% at maximum in the case of efficiency and acceptance correction combined.
- A self-consistency check of the efficiency correction allows us to estimate the uncertainty of the correction procedure to 10% or less. It reflects the difference between the reconstructed distributions after applying all corrections and the simulated original spectra.
- Normalization to the number of π^0 contributes 10% uncertainty.
- The uncertainty of the η yield, calculated bin by bin, is 5% at maximum. This uncertainty is included only for those spectral bins where the η was actually subtracted.
- Uncertainty of the measured NN reference spectra. This contribution, calculated bin by bin, is 20% in the π^0 region and besides this has a maximum of 10% at an invariant mass around 0.5 GeV c^{-2}, where the difference between the reference and the Au + Au spectra is smallest. This uncertainty is included only for those spectra where the reference was actually subtracted.

All systematic uncertainties were finally added in quadrature to obtain the total systematic uncertainty as a function of M_{ee}.

Data availability

All data shown in figures are publicly available from HEPdata (https://hepdata.net/).

Code availability

The HADES raw data have been analysed with the ROOT-based customized reconstruction software HYDRA and stored in data summary files. Detailed information on the analysis procedures employed can be provided by the authors on request.

References

47. Agakishiev, G. et al. The High-Acceptance Dielectron Spectrometer HADES. *Eur. Phys. J. A* **41**, 243–277 (2009).
48. Adamczewski-Musch, J. et al. Centrality determination of Au + Au collisions at 1.23 A GeV with HADES. *Eur. Phys. J. A* **54**, 85 (2018).
49. Harabasz, S. *Reconstruction of Virtual Photons from Au + Au Collisions at 1.23 GeV/u*. PhD Thesis, Tech. Univ. Darmstadt and Jagiellonian Univ. Cracow (2017).
50. Hocker, A. et al. TMVA, the Toolkit for Multivariate Data Analysis with ROOT. PoS(ACAT)040 (2007).
51. Sellheim, P. *Reconstruction of the Low-Mass Dielectron Signal in 1.23 A GeV Au + Au Collisions*. PhD Thesis, Goethe-Univ. Frankfurt (2017).
52. Fröhlich, I. et al. Design of the Pluto Event Generator. *J. Phys. Conf. Ser.* **219**, 032039 (2010).
53. Averbeck, R. et al. Neutral pions and eta mesons as probes of the hadronic fireball in nucleus-nucleus collisions around 1-A-GeV. *Phys. Rev. C* **67**, 024903 (2003).
54. Adamczewski-Musch, J. et al. Deep sub-threshold ϕ production in Au + Au collisions. *Phys. Lett. B* **778**, 403–407 (2018).

The HADES Collaboration

J. Adamczewski-Musch[1], O. Arnold[2,3], C. Behnke[4], A. Belounnas[5], A. Belyaev[6], J. C. Berger-Chen[2,3], J. Biernat[7], A. Blanco[8], C. Blume[4], M. Böhmer[3], P. Bordalo[8], S. Chernenko[6,23], L. Chlad[9], C. Deveaux[10], D. Dittert[11], J. Dreyer[12], A. Dybczak[7], E. Epple[2,3], L. Fabbietti[2,3], O. Fateev[6], P. Filip[13], P. Fonte[8,20], C. Franco[8], J. Friese[3], I. Fröhlich[4], T. Galatyuk[1,11], J. A. Garzón[14], R. Gernhäuser[3], M. Golubeva[15], R. Greifenhagen[12,21], F. Guber[15], M. Gumberidze[1,11], S. Harabasz[7,11], T. Heinz[1], T. Hennino[5], S. Hlavac[13], C. Höhne[10], R. Holzmann[1], A. Ierusalimov[6], A. Ivashkin[15], B. Kämpfer[12,21], T. Karavicheva[15], B. Kardan[4], I. Koenig[1], W. Koenig[1], B. W. Kolb[1], G. Korcyl[7], G. Kornakov[11], R. Kotte[12], A. Kugler[9], T. Kunz[3], A. Kurepin[15], A. Kurilkin[6], P. Kurilkin[6], V. Ladygin[6], R. Lalik[7], K. Lapidus[2,3], A. Lebedev[16], L. Lopes[8], M. Lorenz[4], T. Mahmoud[10], L. Maier[3], A. Mangiarotti[8], J. Markert[1], S. Maurus[3], V. Metag[10], J. Michel[4], D. M. Mihaylov[2,3], S. Morozov[15,17], C. Müntz[4], R. Münzer[2,3], L. Naumann[12], K. N. Nowakowski[7], M. Palka[7], Y. Parpottas[18,22], V. Pechenov[1], O. Pechenova[1], O. Petukhov[15], J. Pietraszko[1], W. Przygoda[7], S. Ramos[8], B. Ramstein[5], A. Reshetin[15], P. Rodriguez-Ramos[9], P. Rosier[5], A. Rost[11], A. Sadovsky[15], P. Salabura[7], T. Scheib[4], H. Schuldes[4], E. Schwab[1], F. Scozzi[5,11], F. Seck[11], P. Sellheim[4], I. Selyuzhenkov[1,17], J. Siebenson[3], L. Silva[8], Yu. G. Sobolev[9], S. Spataro[18], S. Spies[4], H. Ströbele[4], J. Stroth[1,4*], P. Strzempek[7], C. Sturm[1], O. Svoboda[9], M. Szala[4], P. Tlusty[9], M. Traxler[1], H. Tsertos[19], E. Usenko[15], V. Wagner[9], C. Wendisch[1], M. G. Wiebusch[4], J. Wirth[2,3], Y. Zanevsky[6,24] and P. Zumbruch[1]

[1]GSI Helmholtzzentrum für Schwerionenforschung GmbH, Darmstadt, Germany. [2]Excellence Cluster 'Origin and Structure of the Universe', Garching, Germany. [3]Physik Department E62, Technische Universität München, Garching, Germany. [4]Institut für Kernphysik, Goethe-Universität, Frankfurt, Germany. [5]Institut de Physique Nucléaire, CNRS-IN2P3, Université Paris-Sud, Université Paris-Saclay, Orsay, France. [6]Joint Institute of Nuclear Research, Dubna, Russia. [7]Smoluchowski Institute of Physics, Jagiellonian University of Cracow, Kraków, Poland. [8]LIP—Laboratório de Instrumentação e Física Experimental de Partículas, Coimbra, Portugal. [9]Nuclear Physics Institute, The Czech Academy of Sciences, Rez, Czech Republic. [10]II. Physikalisches Institut, Justus Liebig Universität Giessen, Giessen, Germany. [11]Technische Universität Darmstadt, Darmstadt, Germany. [12]Institut für Strahlenphysik, Helmholtz-Zentrum Dresden-Rossendorf, Dresden, Germany. [13]Institute of Physics, Slovak Academy of Sciences, Bratislava, Slovakia. [14]LabCAF. F. Física, Universidade de Santiago de Compostela, Santiago de Compostela, Spain. [15]Institute for Nuclear Research, Russian Academy of Science, Moscow, Russia. [16]Institute of Theoretical and Experimental Physics, Moscow, Russia. [17]National Research Nuclear University MEPhI (Moscow Engineering Physics Institute), Moscow, Russia. [18]Dipartimento di Fisica and INFN, Università di Torino, Turin, Italy. [19]Department of Physics, University of Cyprus, Nicosia, Cyprus. [20]Present address: ISEC Coimbra, Coimbra, Portugal. [21]Present address: Technische Universität Dresden, Dresden, Germany. [22]Present address: Frederick University, Nicosia, Cyprus. [23]Deceased: S. Chernenko. [24]Deceased: Y. Zanevsky. *e-mail: hades-info@gsi.de